The Effects of Surfactants on the Formation and Evolution of Capillary Waves

Hector D. Ceniceros

*Department of Mathematics. University of California, Santa Barbara California 93106.**

(Dated: September 2, 2002)

Abstract

The effects of surface-active agents on the formation and evolution of small capillary ripples developing in the forward front of short water waves is investigated numerically. The capillary waves, believed to have a significant relevance in the process of wave breaking and the onset of turbulence, accompany the initial development of spilling breakers. A novel hybrid numerical methodology is introduced to couple the full two-fluid Navier-Stokes equations with the free boundary motion and with the surfactant dynamics. The hybrid method uses dynamically adaptive Front-Tracking to accurately represent interfacial quantities and forces and to aid in treating the numerical difficulties associated with surface tension. At the same time the method employs the Level Set approach to efficiently update the material properties of the flow. It is found that the capillaries are dramatically affected by the presence of surfactants. The capillary region is invariably marked by accumulation of surfactants that reduces locally the interfacial tension. The size of the wave roller (bulge) diminishes and both the amplitude and wavelength of the capillary ripples also decrease as interfacial tension gradients increase. When surface convection dominates over diffusion, the accumulation of surfactants in the capillary region intensifies and the roller gets smaller and flatter. Large concentration gradients can be produced and these lead to an spread of vorticity along the spilling breakers as a result of the tangential Marangoni stress. In addition to the full two-phase viscous flow simulations, boundary integral computations of the corresponding potential inviscid flow are also performed to compare and contrast the two models in the case of uniform interfacial tension. Differences between the potential and the viscous flows are observed as soon as the wave steepens and develops high-curvature regions.

PACS numbers: PACS 68.10.-m, 83.50.L, 63.10.Cr, 83.10.Lk

Keywords: capillary waves, spilling breakers, Level Set Method, Front-Tracking, surfactants.

*Electronic address: hdc@math.ucsb.edu; URL: http://www.math.ucsb.edu/~hdc

I. INTRODUCTION

Capillary ripples observed in the forward face of sufficiently steep water waves with short wavelength have significant relevance in the process of wave breaking and the onset of turbulence. It is a capillary phenomenon that accompanies the initial development of spilling breakers which are characterized by the formation of a localized zone around the wave crest where the water surface becomes rough and bubbles and droplets form. Duncan [1] reviews the recent advances in the study of spilling breakers and the pattern of surface-tension dominated ripples. The rich effects of surface tension on free and forced waves are also discussed in a review article by Perlin and Schultz [2].

The formation and striking dynamic evolution of these short (often called parasitic) capillary waves have been remarkably captured by the early experimental work of Ebuchi, Kawamura, and Toba [3] for wind driven waves and by the more recent experiments of Duncan, Philomin, and Wenz [4] for gentle spilling breakers. The experiments show that as the wave steepens a "bulge" (roller) forms in the forward face at the crest. The leading edge of this bulge called the toe marks the formation of a train of small amplitude capillary waves which grows rapidly and subsequently breaks down into a random pattern indicating turbulent flow.

Some understanding of these important phenomenon has also been gained with the theoretical work of Longuet-Higgins [5–8] and collaborators [9–11]. Longuet-Higgins has modeled the phenomenon as a capillary jump [7] in steady inviscid waves and has also addressed the crest instabilities of the almost highest Stokes waves [9–11]. The potential flow computations of Yao, Wang and Tullin [12], Jiang, Lin, Schultz and Perlin [13], and Ceniceros and Hou [14] have also revealed important nonlinear behavior. But as pointed out by Duncan [1] breaking in the viscous flow occurs well before the late stages of development found in the potential boundary integral/element simulations. And both experimental and theoretical work support the importance of the viscous shear. One of the few documented attempts to address this numerically is the work by Mui and Dommermuth [15] who combined potential flow-full viscous flow simulations to study the vorticity distribution associated with the capillary waves. There is a clear need for more full viscous flow simulations.

An outstanding open question is how the presence of surface-active ambient agents called surfactants would affect the formation and dynamic development of the capillary waves.

The nonuniform concentration of surfactants produces surface tension gradients that could have dramatic effects on the surface-tension dominated motion. Because in the real world surfactants are almost always present, this is a question of both practical and fundamental importance. The goal of this work is to present a numerical investigation, the first one to our knowledge, of this problem. As pointed out by Stone and Leal [16], there are two main competing effects associated with the presence of surface-active agents: (i) the concentration of surfactant by convection reduces the surface tension and tends to produce larger interfacial deformations and (ii) the dilution of surfactant due to larger interfacial area increases the surface tension and thus acts opposite to the convection of surfactant.

The numerical simulation of water wave motion with the presence of surface-active agents is a challenging problem. It requires the solution of the incompressible two-phase Navier-Stokes equations with a free boundary coupled with an advection-diffusion equation governing the evolution of the surfactant concentration. To make the problem even more difficult, the water surface has very high curvature points at the toe and in the rest of the capillary ripples whose amplitude and wavelength are very small. Here we introduce a novel hybrid Level Set/Front-Tracking method (LeFT). Dynamically adaptive Front-Tracking is used to accurately represent interfacial quantities and forces and to aid in treating the numerical difficulties associated with surface tension. At the same time the method employs the Level Set approach to efficiently update the material quantities of the flow. The combination of these two typically disjoint approaches to numerical free surface problems allows us to resolve the intricate coupled flow-fluid interface-surfactants dynamics.

Our numerical investigation reveals that the capillaries are dramatically affected by the presence of surfactants. The capillary region is invariably marked by accumulation of surfactants that reduces locally the interfacial tension. The size of the roller diminishes and both the amplitude and wavelength of the capillary ripples also decrease as interfacial tension gradients increase. When surface convection dominates over diffusion, the accumulation of surfactants in the capillary region intensifies and the roller gets smaller and flatter. Large concentration gradients can be produced and these lead to an spread of vorticity along the spilling breakers as a result of the tangential Marangoni stress.

In addition to the full two-phase viscous flow simulations, boundary integral computations of the corresponding potential inviscid flow are also performed to compare and contrast the two models in the case of uniform interfacial tension. Differences between the potential and

the viscous flows are observed as soon as the wave steepens and develops high-curvature regions. Rotational and viscous effects, as well as the presence of a second phase appears to have a noticeable influence in the fully nonlinear flow.

The rest of the paper is organized as follows. The equations of motion are introduced in Section II. Section III is devoted to the presentation of the numerical methodology and its implementation. A numerical validation is given in Section IV. The numerical study is presented in Section V. This is followed by some concluding remarks and comments for ongoing and future work.

II. THE GOVERNING EQUATIONS

We model the wave motion as that of a free interface separating two incompressible immiscible fluids (labeled 1 and 2) with air-water viscosities and densities ratios in two dimensions. We assume that the flow is periodic in the horizontal direction and that it is limited by walls (with slip boundary condition) in the vertical direction. The starting point is thus the Navier-Stokes equations for each phase:

$$\frac{\partial \mathbf{u}_i}{\partial t} + \mathbf{u}_i \cdot \nabla \mathbf{u}_i = -\frac{1}{\rho_i}\nabla p_i + \frac{1}{\rho_i}\nabla \cdot \mu_i(\nabla \mathbf{u}_i + \nabla \mathbf{u}_i^T) - g\mathbf{j}, \tag{1}$$

$$\nabla \cdot \mathbf{u}_i = 0, \tag{2}$$

where $\mathbf{u}_i$, p_i, ρ_i and μ_i $(i = 1, 2)$ are the velocity field, the pressure, the density, and the viscosity of each fluid respectively, and g is the gravity acceleration constant. At the fluid interface, the surface stress satisfies the jump condition:

$$-(p_2 - p_1)\hat{\mathbf{n}} + (\mathbf{S_2} - \mathbf{S_1})\hat{\mathbf{n}} = -\sigma\kappa\hat{\mathbf{n}} - \nabla_s\sigma, \tag{3}$$

where $\hat{\mathbf{n}}$ is the unit normal pointing into Fluid 2, $\mathbf{S_i} = \mu_i(\nabla \mathbf{u}_i + \nabla \mathbf{u}_i^T)$ is the viscous stress tensor, σ the surface tension coefficient, κ is the mean curvature and ∇_s is the surface gradient. Figure 1 gives a schematic of the problem and the definition of the tangential and normal vectors, and the curvature. $\nabla_s\sigma$ represents the Marangoni stress resulting from a non-uniform surface tension.

The interfacial tension σ depends on the surface concentration Γ^* of surfactant and is given by an equation of state of the form $\sigma = \sigma(\Gamma^*)$. We assume that initially there is a uniform concentration of surfactant Γ_0 (measured in units of surfactant mass per unit area).

Letting $\Gamma = \Gamma^*/\Gamma_0$ the equation of state can be written as [17]:

$$\sigma(\Gamma) = \sigma_s(1 - \beta\Gamma), \tag{4}$$

where σ_s is the surface tension of the clean surface and β, which satisfies $0 \leq \beta \leq 1$, is a physico-chemical dimensionless parameter that measures the sensitivity of surface tension to changes in surfactant concentration. The equation of state (4) has been used by Stone and Leal [16], by Pozrikidis [18], and by Siegel [19] in the context of Stokes bubbles.

The changes in the surfactant concentration at the fluid interface are governed by a convection-diffusion equation that can be written as [20]:

$$\left.\frac{\partial \Gamma}{\partial t}\right|_{\alpha} = \frac{\partial \mathbf{X}}{\partial t} \cdot \nabla_s \Gamma - \nabla_s \cdot (\Gamma \mathbf{u}_s) + \Gamma \kappa \mathbf{u} \cdot \hat{\mathbf{n}} + D_s \nabla_s^2 \Gamma, \tag{5}$$

where $\mathbf{u}_s$ represents the velocity vector tangent to the fluid interface, $\mathbf{X}(\alpha, t)$ is a parametrization of the interface, and D_s is the surface diffusivity. We consider the surfactant to be insoluble so there is no net flux of the surface-active material to and from the interface from the bulk phases. Finally a kinematic boundary condition is imposed on the fluid interface. The normal velocity $U^N \hat{\mathbf{n}}$ of a point on the fluid interface equals the corresponding velocity of the fluid evaluated at the interface:

$$U^N \hat{\mathbf{n}} = \hat{\mathbf{n}}(\mathbf{u} \cdot \hat{\mathbf{n}}). \tag{6}$$

III. THE NUMERICAL METHOD

A. A Hybrid Level Set-Front Tracking Approach

The need to accurately compute interfacial forces and to resolve the short and high-curvature capillary train makes Front-Tracking based methods the most suitable for this type problem. In Front-Tracking methods [21] the interface is tracked by a separate grid (surface markers) on a lower dimension. Thus, such methods would be a natural choice also on the account that the surfactants reside and change dynamically only on the fluid interface and not in the bulk phases.

Typically in multiphase flow simulations the different phases are treated as one fluid with variable material properties (density and viscosity). In the Front-Tracking setting these quantities are often updated by solving a Poisson equation [22] at every time-step. However

this procedure produces occasionally erroneous values away from the interface and small over- and under-shoots [22]. This situation is particularly aggravated when there are high density ratios as is the case for an air-water system whose density ratio is $O(10^3)$. The Level Set Method [23] offers a more natural and *smoother* fluid indicator than the largely discontinuous density (or the viscosity). In this method the fluid interface is embedded as the zero level set of a "color" function ϕ that, when re-initialized properly [24], defines at all times a signed distance function to the interface. Moreover the evolution of ϕ can be captured accurately and at optimal cost using the well-established numerical methodology for conservation laws. Here we propose to combine the Level Set Method, normally used as an interface-capturing tool, with Front-Tracking to obtain a hybrid Level Set Method/Front-Tracking (LeFT) method that exploits some of the best features of each individual approach. The rationale is that the accurate computation of interfacial quantities via Front-Tracking leads to more accurate velocity fields which in turn produce more accurate updates of the bulk fluid material quantities obtained via the Level Set Method. Moreover, as will be discussed later, the use of adaptive Front-Tracking allows us to relax a numerical difficulty associated with surface tension.

To describe the method we first rewrite the equations of motion using the immersed boundary (δ function) setting [25] to account for the stress jump condition (3) and add the level set equation and an evolution equation for the interface position. In dimensionless form the governing equations become:

$$\phi_t + \mathbf{u}\cdot\nabla\phi = 0, \tag{7}$$

$$\mathbf{u}_t + \mathbf{u}\cdot\nabla\mathbf{u} = -\frac{1}{\rho(\phi)}\nabla p + \frac{1}{Re\rho(\phi)}\nabla\cdot\mu(\phi)(\nabla\mathbf{u}+\nabla\mathbf{u}^T) - \frac{\mathbf{j}}{Fr} + \mathbf{F}, \tag{8}$$

$$\mathbf{F}(\mathbf{x}) = \frac{1}{We\rho(\phi)}\int\frac{\partial(\sigma\hat{\mathbf{t}})}{\partial\alpha}\delta(\mathbf{X}(\alpha,t)-\mathbf{x})d\alpha, \tag{9}$$

$$\nabla\cdot\mathbf{u} = 0, \tag{10}$$

$$\mathbf{X}_t(\alpha,t) = \int\mathbf{u}(\mathbf{x})\delta(\mathbf{x}-\mathbf{X}(\alpha,t))d\mathbf{x}, \tag{11}$$

where ϕ is the level set function ($\phi = 0$ for the points on the interface, $\phi > 0$ for water and $\phi < 0$ for air). The position of the fluid interface is specified in parametric form by $\mathbf{X}(\alpha,t)$ and $\hat{\mathbf{t}}$ is the unit tangent vector to the interface. δ is the two-dimensional delta function. Note that the normal surface tension and the Marangoni stress have been combined into one term [22] using the Frênet formula $\partial_s\hat{\mathbf{t}} = \kappa\hat{\mathbf{n}}$, where ∂_s denotes derivative with respect

to arclength.

In the nondimensionalization, the three dimensionless flow parameters are the Reynolds number Re, the Froude number Fr, and the Weber number We defined as:

$$Re = \frac{\rho_{\text{water}} \lambda U_c}{\mu_{\text{water}}}, \qquad Fr = \frac{U_c^2}{g\lambda}, \qquad We = \frac{\rho_{\text{water}} \lambda U_c^2}{\sigma_s},$$

where λ is the wavelength and U_c is a characteristic velocity. Here we take $Fr = 1$ so that the velocity scale is given by $U_c = \sqrt{g\lambda}$. Thus, the dimensionless wavelength is 1 and the linear wave period T is $\sqrt{2\pi}$.

The dimensionless density and viscosity are given by:

$$\rho(\phi) = r + (1 - r)H(\phi), \tag{12}$$

$$\mu(\phi) = \eta + (1 - \eta)H(\phi), \tag{13}$$

where $r = \rho_{\text{air}}/\rho_{\text{water}} = 1.2 \times 10^{-3}$ and $\eta = \mu_{\text{air}}/\mu_{\text{water}} = 1.57 \times 10^{-2}$ and $H(\phi)$ is the Heaviside function defined by

$$H(\phi) = \begin{cases} 0 & \text{If } \phi < 0, \\ \frac{1}{2} & \text{If } \phi = 0, \\ 1 & \text{If } \phi > 0. \end{cases} \tag{14}$$

Note that, as remarked above, ϕ is only used to obtain ρ and μ through (12)-(14) but the interface and the surface tension force $\rho\mathbf{F}$ are computed directly from $\mathbf{X}(\alpha, t)$.

The dimensionless surface tension σ is given by the equation of state

$$\sigma(\Gamma) = 1 - \beta\Gamma. \tag{15}$$

Equations (7)-(15) are coupled to the convection-diffusion equation of the surfactant concentration (5). We discuss next a computationally efficient frame for the front-particle motion and rewrite (5) using this frame.

B. Dynamically Adaptive Front-Tracking: Particle Equidistribution

The short capillary waves on the front of water waves develop regions of very high curvature, a feature shared by other important multi-phase fluid applications. While Front-Tracking methods allow us to better capture these high curvature regions, it is well known

that in Front-Tracking methods the surface marker particles develop excessive clustering, often at the wrong places [26]. And as a result, regridding algorithms (static point insertion and deletion) are usually employed to redistribute the particles to avoid poor overall resolution and a prohibitively small time step.

In the context of boundary integral methods Baker and Nachbin [26] note that keeping the surface particles approximately equidistributed in arc-length relaxes significantly the surface tension-induced time step constraint of an explicit method. Also in the context of boundary integral methods Hou, Lowengrub, and Shelley [27] use particle equidistribution as one of the main ingredients to efficiently remove the numerical stiffness associated with surface tension.

Following these observations we change the interface parametrization dynamically to enforce surface particle equidistribution. The kinematic condition (6) gives us room to introduce an arbitrary tangential velocity in (11) so that the evolution equation for $\mathbf{X}$ becomes:

$$\mathbf{X}_t(\alpha,t) = \int \mathbf{u}(\mathbf{x})\delta(\mathbf{x}-\mathbf{X}(\alpha,t))d\mathbf{x} + U^A\hat{\mathbf{t}} \equiv \mathbf{U}(\alpha,t) + U^A\hat{\mathbf{t}}, \tag{16}$$

where U^A is arbitrary and determines the frame or parametrization used to describe the interface. It can be easily shown that if the particles are initially equidistributed in arc-length they will be kept so if [27]

$$U^A = -U^T + \int_0^\alpha [s_\alpha \kappa U^N - < s_\alpha \kappa U^N >]d\alpha', \tag{17}$$

where $U^T = \mathbf{U}\cdot\hat{\mathbf{t}}$, $s_\alpha = \sqrt{X_\alpha^2 + Y_\alpha^2}$, κ is the mean curvature, and $< \cdot >$ stands for the spatial mean (over one spatial period).

Using this dynamic parametrization the convection-diffusion equation governing the evolution of the surfactant concentration can be written in dimensionless form as:

$$\left.\frac{\partial\Gamma}{\partial t}\right|_\alpha = \left(\frac{U^T+U^A}{s_\alpha}\right)\frac{\partial\Gamma}{\partial\alpha} - \frac{1}{s_\alpha}\frac{\partial(\Gamma U^T)}{\partial\alpha} + \Gamma\kappa U^N + \frac{1}{P_e}\frac{1}{s_\alpha}\frac{\partial}{\partial\alpha}\left(\frac{1}{s_\alpha}\frac{\partial\Gamma}{\partial\alpha}\right), \tag{18}$$

where $U^N = \mathbf{U}\cdot\hat{\mathbf{n}}$, $U^T = \mathbf{U}\cdot\hat{\mathbf{t}}$, and $P_e = \lambda U_c/D_s$ is the Péclet number that measures the importance of convection relative to diffusion.

C. Time Integration and Implementation

Finally, to discretize the full coupled system of equations (7)-(18) we replace the delta and the Heaviside functions by mollified versions. Here we choose Peskin's delta function [25]

$$\delta_\epsilon(x) = \begin{cases} \frac{1}{2\epsilon}[1+\cos\frac{\pi x}{\epsilon}] & \text{If } |x| \le \epsilon, \\ 0 & \text{Otherwise,} \end{cases} \tag{19}$$

and

$$H_\epsilon(x) = \begin{cases} 0 & \text{If } x < -\epsilon, \\ \frac{1}{2}[1+\frac{x}{\epsilon}+\frac{1}{\pi}\sin\frac{\pi x}{\epsilon}] & \text{If } |x| \le \epsilon, \\ 1 & \text{If } x > \epsilon, \end{cases} \tag{20}$$

where ϵ is a numerical parameter depending on the Eulerian grid mesh size Δx. For the computations reported here $\epsilon = 2\Delta x$. Note that $\frac{dH_\epsilon}{dx} = \delta_\epsilon$.

We describe next one Euler step of the time discretization scheme. The spatial discretization is standard second order except for the convection terms which are discretized using a third order ENO scheme. First, the fluid interface position, the surfactant concentration, and the level set function are updated:

$$\mathbf{X}^{n+1} = \mathbf{X}^n + \Delta t[(U^{T,n}+U^{A,n})\hat{\mathbf{t}}^n + U^N\hat{\mathbf{n}}^n], \tag{21}$$

$$\Gamma^{n+1} = \Gamma^n + \Delta t\frac{1}{P_e}\frac{1}{s_\alpha^{n+1}}\frac{\partial}{\partial\alpha}\left(\frac{1}{s_\alpha^{n+1}}\frac{\partial\Gamma^{n+1}}{\partial\alpha}\right) + \Delta t G^n, \tag{22}$$

$$\phi^{n+1} = \phi^n - \Delta t(\mathbf{u}^n\cdot\nabla\phi^n), \tag{23}$$

where G^n stands for the right hand side of (18) minus the diffusion term, evaluated at the n-th time-step. With the standard second order spatial discretization Equation (22) can be solved efficiently for Γ^{n+1} with a tridiagonal solver. The nonuniform surface tension $\sigma(\Gamma^{n+1})$ is evaluated using the equation of state (15) and the interfacial tension term (9) is computed. Using this force the velocity field is updated with the Projection Method on a staggered MAC grid in the standard two-stage process [28]:

$$\frac{\mathbf{u}^*-\mathbf{u}^n}{\Delta t} = -\mathbf{u}^n\cdot\nabla\mathbf{u}^n + \frac{1}{Re\rho^n}\nabla\cdot\mu^n(\nabla\mathbf{u}^n+\nabla\mathbf{u}^{nT}) - \frac{\mathbf{j}}{Fr} + \mathbf{F}^{n+1}, \tag{24}$$

$$\frac{\mathbf{u}^{n+1}-\mathbf{u}^*}{\Delta t} = -\frac{1}{\rho^{n+1}}\nabla p^{n+1}, \tag{25}$$

where, to enforce the incompressibility condition $\nabla\cdot\mathbf{u}^{n+1}$, p^{n+1} is the solution of the equation

$$\nabla\cdot\left(\frac{1}{\rho^{n+1}}\nabla p^{n+1}\right) = \frac{1}{\Delta t}\nabla\cdot\mathbf{u}^*, \tag{26}$$

with homogeneous Neumann boundary conditions at walls and periodic in the horizontal direction. To solve this elliptic equation we employ the Conjugate Gradient Method (CG) preconditioned with a robust multigrid method that uses matrix dependent prolongation [29]. This particular multigrid handles efficiently discontinuous and high contrast coefficients and convergences rapidly even for the very high density ratio (10^3) of this problem. The CG method corrects locally the solution to enforce the horizontal periodic boundary conditions. The multi-grid preconditioned CG converges within truncation error typically in less than 10 iterations. Note that the viscous term is treated explicitly as for high Reynolds numbers such as the one considered here the explicit treatment is more efficient computationally.

Following Kang, Fedkiw, and Liu [30] we embed the Euler step into a third order total variation diminishing (TVD) Runge-Kutta [31] as follows. Denoting the Euler step by $E(\mathbf{V})$ where $\mathbf{V}$ stands for all the dynamic variables we obtain [30]

$$\mathbf{V}^{n+1} = \frac{1}{3}\mathbf{V}^n + \frac{2}{3}E\left(\frac{3}{4}\mathbf{V}^n + \frac{1}{4}E(E(\mathbf{V}^n))\right). \tag{27}$$

Being the scheme a one-step method, adaptive time stepping can be implemented naturally. Finally, we note that the level set function ϕ is re-initialized with the procedure described in [24] to maintain it as a signed distance function. Also a fourth order filter [32]: $\mathbf{X}_j \leftarrow \frac{1}{16}(-\mathbf{X}_{j-2} + 4\mathbf{X}_{j-1} + 10\mathbf{X}_j + 4\mathbf{X}_{j+1} - \mathbf{X}_{j+2})$ is applied every time step to the interface position to eliminate the small amplitude mesh-scale oscillations characteristic of the immersed boundary setting. In the numerical experiments the overall LeFT method is very stable and robust. In particular, the interfacial tension-induced constraint enhanced by excessive particle clustering has been relaxed. A more detailed study of the method will be presented elsewhere.

IV. NUMERICAL VALIDATION

Given that the numerical methodology employed here is new we conduct first a numerical validation. In view of the lack of results for nonuniform tension capillary waves, we consider the case of constant surface tension. This also allows us to compare with inviscid potential flow boundary integral simulations. Furthermore, to compare also with experimental results we follow Jiang, Lin, Schultz, and Perlin [13] and select initial conditions that approximate those produced in the laboratory with a flap-type wavemaker following a sinusoidal motion.

In particular, we consider the linear wave initial conditions in [13], $\xi = ka\cos(kx)$ and $\phi = ka\sin(kx)$, where ξ and ϕ are the initial free surface elevation and velocity potential respectively and ka is the wave steepness. In our dimensionless variables, the initial wave profile is given in parametric form by

$$X(\alpha, 0) = \alpha, \tag{28}$$

$$Y(\alpha, 0) = A\cos(2\pi\alpha), \tag{29}$$

for $0 \leq \alpha \leq 1$ and where $2\pi A$ is the wave steepness. The initial velocity potential is $\phi = \frac{A}{\sqrt{2\pi}}\sin(2\pi\alpha)$. To obtain the initial velocity in the whole computational domain from free surface-defined ϕ we proceed as follows. First, we compute the (unnormalized) vortex sheet strength γ by solving the integral equation [14]

$$\phi_\alpha(\alpha) = \frac{1}{2}\gamma(\alpha) + \Re\left\{\frac{Z_\alpha(\alpha)}{2i}\int_0^1 \gamma(\alpha')\cot\pi[Z(\alpha) - Z(\alpha')]d\alpha'\right\}, \tag{30}$$

where $Z(\alpha) = X(\alpha) + iY(\alpha)$ and $\Re$ stands for the real part. The solution γ is computed via fixed point iteration using a spectral discretization as described in [14].

With γ known, the initial vorticity ω_0 in the whole domain is given by

$$\omega_0(\mathbf{x}) = \int_0^1 \gamma(\alpha)\delta(\mathbf{X}(\alpha) - \mathbf{x})d\alpha. \tag{31}$$

Then, the stream function ψ is found by solving numerically (with standard second order finite differences) the Poisson's equation

$$\Delta\psi = -\omega_0, \tag{32}$$

with periodic boundary conditions in the streamwise direction and Dirichlet homogeneous conditions in the vertical direction. Finally, the initial velocity is computed from ψ using

$$u_0 = \psi_y, \tag{33}$$

$$v_0 = -\psi_x, \tag{34}$$

with centered differences.

Figure 2 shows the profile of a wave with initial steepness $2\pi A = 0.2$, $We = 4\pi^2/0.07$ ($\lambda = 6.5$ cm, as in [13]), and $Re = 45627$ at times $t = T$ and $t = \frac{11}{8}T$. $T = \sqrt{2\pi}$ is the dimensionless linear wave period. Two resolutions (continuous curve), 512×512 with

512 interface markers and 1024×1024 with 1024 interface markers, are plotted in the same figure. Also shown in Figure 2 (dashed-dotted curve) is the corresponding profile for inviscid infinite depth potential flow. This inviscid profile is computed with the boundary integral method described in [14] and matches that shown in Fig. 2 in [13]. The vertical scale is eight times the horizontal one as in [13]. The two resolutions of the full two-fluid Navier-Stokes flow give profiles that are indistinguishable within plotting resolution. At $t = T$ [Fig. 2(a)], also the inviscid profile is very close to the viscous one. At $t = \frac{11}{8}T$ [Fig. 2(b)], a more significant difference can be observed between the inviscid potential flow profile and the two-fluid viscous profiles. The amplitudes of the wave and the capillaries in the viscous flow are smaller than those in the potential flow. It is unlikely that this is due to underresolution of the viscous simulations as the profiles computed with the two different resolutions almost coincide. Thus, Fig. 2(b) shows in effect the difference between the potential flow and the two-fluid viscous flow when the capillary waves are fully developed. Rotational and viscous effects, as well as the presence of a second phase have a noticeable influence in the fully nonlinear flow. The viscous profiles compare well with the experiments in [13] for initial steepness equal to 0.19, Fig. 13(a) in [13].

V. THE NUMERICAL EXPERIMENTS

A. Initial Conditions

For our study we focus now on a wave similar to the wind generated spilling breakers investigated experimentally by Ebuchi *et al.* [3]. The wave has initial steepness $2\pi A = 0.335$ as in [3]. $Fr = 1$ as before but we take now $We = 980$ which corresponds to a wavelength of 8.53cm. We keep the same Reynolds number, $Re = 45627$, to afford resolve the viscous boundary layer thickness $\sim \sqrt{1/Re}$ (the actual Reynolds number is higher). The initial position of the fluid interface is given again by (28)-(29) but now there is a uniformly concentrated vorticity distribution initially at the fluid interface (a vortex sheet): $\gamma \equiv -1/\sqrt{9.8}$. The initial velocity is obtained from (31)-(34).

The full two-phase viscous flow simulations are computed with the hybrid LeFT method as follows. A 512×512 mesh with 512 interface markers is used to compute up to $t = 0.8T$. Then, linear interpolation is performed and the computations are continued from $t = 0.8T$

to $t = T$ with a 1024×1024 mesh and 1024 interface markers. The time $t = 0.8T$ was selected because the capillary waves are not yet fully developed and the flow can be resolved with the coarser mesh. The accuracy and resolution were assessed by comparing the profiles computed with the two different meshes. The profiles coincided within plotting resolution at $t = 0.8T$ and the maximum difference in $Y(\alpha)$ at $t = T$ was less than 2×10^{-3}.

B. Uniform Surface Tension

In the absence of surfactants $\Gamma = 0$ and the surface tension remains constant in space and time. Figure 3 shows the evolution of the wave at different times. The corresponding potential flow profile, computed with the boundary integral method, has also been plotted (dashed-dotted curve) before and after the formation of the capillary waves for comparison. A hump develops around $x = 0.4$ and reaches maximum height at about $t = 0.48T$. A slight difference between the potential flow profile and the full two-phase viscous flow profile can already be seen at this early time. When the hump falls, the mass of water creates a right-moving wave and a small bulge ending in a point of growing curvature (the toe) emerges around $t = 0.82T$ forming a bore-like structure. At this time a train of fairly small amplitude capillary waves begins to be visible on the leading side of the toe. The main wave reaches a maximum height around $t = T$ after which it begins to fall again. The wavelength of the capillary waves at $t = T$, estimated from the first two curvature maxima is 0.056. The potential and the full two-phase viscous profiles differs noticeably at $t = T$ precisely at the roller-capillary region which is characterized by large curvature points. It is not unreasonable that both rotational and viscous effects may play a significant role there.

Figure 4 depicts the vorticity field before and after the formation of the short capillary waves. At $t = 0.4T$ before the onset of the capillaries, the vorticity extrema occur at the front and back of the wave crest. The vorticity remains fairly concentrated at the free surface but a small negative amount has already been shed into the air side in the immediate vicinity of the fluid interface. With the capillaries fully developed at $t = T$, the bulge (roller) preceding them is characterized by a region of high vorticity ($\max \omega = 73$) as observed in the wind-tunnel experiments of Okuda [33]. The toe has fairly large curvature and the vorticity achieves its largest absolute value $\min \omega = -247$ precisely at the toe. This is consistent with Longuet-Higgins [34] observation that the vorticity is proportional to the curvature

for a steady flow in which the tangential stress vanishes. The structure of the capillaries can be better appreciated in Figure 5 which provides closeups of vorticity contours and the curvature around the capillary region at $t = T$. The location of the free surface in Figure 5(a) is marked by a dashed-dotted curve.

C. The Effects of Surfactants

There are two parameters associated with the presence of the surface-active agents and their dynamics. The physico-chemical parameter β which determines the sensitivity of interfacial tension to changes in surfactant concentration Γ and the Péclet number Pe. We illustrate the effects of these parameters on the flow in Figs. 6-8. The figures show (a) a comparison of the wave profile in the presence of surfactants and the corresponding clean-surface profile (dotted line) at $t = T$, (b) the curvature of the surfactant-affected surface also at $t = T$, and (c) the surfactant concentration at $t = 0$, $t = 0.8T$, and $t = T$. Figure 6 and Fig. 7 share the same Péclet number ($Pe = 1$) but different β, 0.5 and 0.7 respectively, while Fig. 8 presents results for $\beta = 0.7$ and a higher Péclet number ($Pe = 10$). All the computations begin at $t = 0$ with a uniform surfactant concentration $\Gamma = 1$.

As it is evident from the wave profiles, the presence of surfactants reduces the size of the roller and the amplitude of the capillary waves. This is accompanied by an increased curvature at the toe. In the case of $Pe = 1$ (Figs. 6 and 7), surface diffusion dominates and the surfactant concentration develops only a relatively small variation with respect to the initial uniform value. Nevertheless, it can be clearly observed in box (c) of Figs. 6 and 7 that the flow leads to an accumulation of surfactant around the main-wave crest with a concentration peak at the toe. Furthermore, as the fluid interface stretches, during $t = 0.8T$-T, the surfactant is diluted and its concentration becomes less than one. At the continuous level the total amount of surfactants must remain constant in time. Following Stone and Leal [16] the local surfactant concentration is rescaled every time step to enforce this requirement. The wavelength of the capillary waves at $t = T$ for $Pe = 1$, estimated from the first two curvature maxima, is 0.033 for $\beta = 0.5$ and 0.023 for $\beta = 0.7$, significantly smaller than that in the clean-surface flow (0.056). Thus, as expected from the reduction in interfacial tension, the surfactants also produce a decrease in the capillary wavelength.

In the case of $Pe = 10$ (Fig. 8), there is a stronger flow convection transporting the

surfactant toward the crest and producing a larger variation in the concentration. Note in particular that for this Péclet number the concentration is greater than one in the capillary region at $t = T$ and the wave profile shows a less rounded roller with a smaller toe curvature than that for $Pe = 1$ and the same β (Fig. 7). Furthermore, the main wave height is visibly smaller for $Pe = 10$. This is not merely a delay in the dynamics induced by the surfactants as both waves have reached their maximum height and are already beginning to fall down at $t = T$ (longer time dynamics will be addressed in the next subsection). The wavelength of the capillary waves for $Pe = 10$, $\beta = 0.7$ at $t = T$ is 0.024. In summary, for a small fixed Péclet number the size of the roller appears to decrease and both the amplitude and wavelength of the capillary waves also decrease as the physico-chemical parameter β increases. For a fixed β, an increase in the Péclet number intensifies the transport and the accumulation of surfactants in the capillary region, reducing there the interfacial tension and producing a less deformed roller and a wave with a smaller height.

We can gain some understanding of the observed effects of surfactants if, following Stone and Leal [16], we let $\Gamma = 1+\Gamma'$ where Γ' is a small perturbation of the uniform concentration equal to one, and then write the stress balance at the free surface as:

$$-(p_2 - p_1)\hat{\mathbf{n}} + \frac{1}{Re}(\mathbf{S_2} - \mathbf{S_1})\hat{\mathbf{n}} = -\frac{1}{We^*}\kappa\hat{\mathbf{n}} + \frac{\beta}{We^*(1-\beta)}[\Gamma'\kappa\hat{\mathbf{n}} + \nabla_s\Gamma'], \tag{35}$$

where

$$We^* = \frac{We}{1-\beta}, \tag{36}$$

is an effective Weber number. The first term on the right hand side of (35) corresponds to the usual normal surface tension force but with an increased Weber number We^*. The second term modifies this force only slightly for $\beta|\Gamma'|/(1-\beta)$ small, as it turned out to be in the cases we have considered so far. But Marangoni term $\beta\nabla_s\Gamma'/(1-\beta)$, last term on the right hand side of (35), may have a significant contribution if large concentration gradients occur due to the flow transport of surfactants. As we have seen, for small Péclet numbers, the surfactant concentration develops only small variations around the uniform value one. Thus, the dominant effect of surfactants is to decrease the surface tension from σ_s to $\sigma^* = \sigma_s(1-\beta)$. Consequently, for small Péclet numbers the evolution of the free surface with interfacial tension gradients can be expected to be close to that with constant surface tension σ^* and Weber number We^*.

Figure 9 shows a comparison of the $\beta = 0.7$ variable interfacial tension profiles, $Pe = 1$

(dashed curve) and $Pe = 10$ (dashed-dotted curve), with the constant surface tension $We^* = We/(1-0.7)$ profile (continuous curve). For $Pe = 1$ the free surface almost coincides with the constant tension We^* interface with the largest deviation occurring at the leading portion of the roller. The wavelength of the capillary waves in the constant tension We^* flow is 0.022 which is about the same as that observed in the $\beta = 0.7$ profiles. There is however an appreciable difference in the roller-capillary region between the We^* flow and the $Pe = 10$, $\beta = 0.7$ flow. As noted before, when the Péclet number is increased, convection leads to a larger accumulation of surfactants in the roller-capillary region and thus decreasing the surface tension there. At the same time larger concentration gradients are generated and these bring into play the tangential Marangoni stress. As a result of this complex flow dynamics a less deformed roller and a reduced wave height are produced but the wavelength of the capillaries does not seem to be significantly affected.

To investigate further the effect of the Marangoni term we consider now a much larger Péclet number, $Pe = 100$, keeping $\beta = 0.7$. The results are summarized in Fig. 10. Figure 10(a) compares the capillary region with the one obtained for $Pe = 1$ and $Pe = 10$ while Fig 10(b) shows the surfactant concentration of the $Pe = 100$ flow at $t = T$ (plotted with equal aspect ratio). The largest Péclet number profile shows an even flatter and smaller crest than that for $Pe = 10$. The surfactant has been swept toward the crest and the forward front of the wave while being diluted at the back. Moreover, a sharp variation of the surfactant concentration around the crest ($\sim x = 0.7$) is observed. The resulting effect is that that capillary ripples have been completely inhibited up to this time.

One of the effects of the tangential Marangoni stress can also be seen in the vorticity fields of the studied flows presented in Figure 11. Just as in the absence of surfactants, a strong concentration of vorticity at the roller and toe is observed in Fig. 11(a)-(c). The vorticity at time $t = T$ is still fairly confined to the fluid interface but a small amplitude vorticity can be seen in a vicinity of the free surface at both fluids. The $Pe = 100$, $\beta = 0.7$ flow, for which a strong Marangoni effect is expected, presents a large vorticity at the crest but the field is more uniformly spread along stretched regions at the back and front of the wave. This a clear indication of the tangential stress generated by the variable interfacial tension.

D. Longer Time Dynamics

For $\beta = 0.7$ and $Pe = 100$ the complex coupled surfactant-flow dynamics inhibited the formation of capillary ripples up to $t = T$. It is natural to ask whether or not the onset of the capillary waves will occur at a later time. To address this question we look a longer time dynamics for both the $\beta = 0.7$, $Pe = 100$ flow and the clean-surface $We = 980$ flow. Figure 12(a) shows the wave profile of the surfactant-affected flow at three subsequent times. The wave achieves its maximum height shortly before $t = T$ and then the crest begins to fall. At $t = 1.096T$, a well defined toe can now be identified and as the wave continues to drop a very small amplitude first ripple begins to form at $t = 1.197T$. The clean-surface wave has a similar motion except that it is accompanied by the train of capillaries. Figure 12(b) contrasts the differences between the clean-surface flow and the $Pe = 100$ flow at $t = 1.197T$. The surfactants do not merely delay the onset of the capillary ripples but almost completely inhibit them when the flow transport becomes significant. A much longer time simulation using the boundary integral method for the constant interfacial tension potential flow shows that the main wave rises up again and the capillary waves intensify. Unfortunately, similar simulations for the full two-phase viscous flow would too demanding computationally in terms of both increased resolution and CPU time.

Finally, as noted by Jiang, Lin, Schultz, and Perlin [13], the steepness of the capillary ripples appears to be sensitive to variations of the the main wave initial steepness. For the particular initial conditions on which we focused this study we observe, through potential flow simulations, that the steepness of capillary waves tends to increase as the initial steepness is slightly increased.

VI. CONCLUDING REMARKS

The effect of surface-active agents on the formation of short capillary waves has been investigated numerically. The full two-fluid incompressible Navier-Stokes equations coupled with a surface-defined advection-diffusion equation for the surfactant concentration have been solved with a novel numerical approach. The new hybrid methodology combines level set and adaptive Front-Tracking techniques to achieve an accurate and stable treatment of interfacial tension in a multi-phase flow.

Through high-resolution numerical experiments it is found that capillaries are dramatically affected by the presence of surfactants. The capillary region is invariably marked by accumulation of surfactant concentration. For a small fixed Péclet number the size of the roller decreases and both the amplitude and wavelength of the capillary ripples also diminishes as interfacial tension gradients increase. The dominant effect of the surfactants in the flow with strong surface diffusion is a net reduction of the interfacial tension. As the Péclet number is increased the surface transport and the accumulation of surfactants in the capillary region intensify and the roller gets smaller and flatter. Large concentration gradients can be produced as the flow sweeps the surfactants toward the wave front and dilutes them at the back. These gradients lead to an spread of vorticity along the spilling breakers as a result of the tangential Marangoni stress.

Three-dimensional effects during the formation and evolution of the capillary waves remain a mystery. The novel numerical methodology presented here can naturally be extended to three dimensions. This is however a quite challenging computational problem and will be the subject of future work as will be the investigation of much longer time dynamics.

Acknowledgments

The author thanks Prof. J. H. Duncan for suggesting the problem and Prof. C. Garcia-Cervera for stimulating conversations. The author is also grateful to the referees for their valuable comments and suggestions. This work was partially supported by the Faculty Career Development Award grant and the Academic Senate Junior Faculty Award grant.

[1] J. H. Duncan. Spilling breakers. *Annu. Rev. Fluid Mech.*, 33:519–547, 2001.

[2] M. Perlin and W. W. Schultz. Capillary effects on surface waves. *Annu. Rev. Fluid Mech.*, 32:241–274, 2000.

[3] N. Ebuchi, H. Kawamure, and Y. Toba. Fine structure of laboratory wind-waves surfaces studied using an optical method. *Boundary Layer Met.*, 39:133–151, 1987.

[4] J. H. Duncan, H. Qiao, V. Philomin, and A. Wenz. Gentle spilling breakers:crest profile evolution. *J. Fluid Mech.*, 379:191–222, 1999.

[5] M. S. Longuet-Higgins. Shear instability in spilling breakers. *Proc. R. Soc. Lond. A*, 446:399–409, 1994.

[6] M. S. Longuet-Higgins. Parasitic capillary waves: a direct calculation. *J. Fluid Mech.*, 301:79–107, 1995.

[7] M. S. Longuet-Higgins. Capillary jumps on deep water. *Journal of Physical Oceanography*, 26:1957–1965, 1996.

[8] M. S. Longuet-Higgins. Progress toward understanding how waves break. In *Twenty-First Symposium on Naval Hydrodynamics*, pages 7–28, Washington D. C., 1997. National Academy Press.

[9] M. S. Longuet-Higgins and R. P. Cleaver. Crest instabilities of gravity waves. Part 1. The almost highest wave. *J. Fluid Mech.*, 258:115–129, 1994.

[10] M. S. Longuet-Higgins, R. P. Cleaver, and M. J. H. Fox. Crest instabilities of gravity waves. Part 2. *J. Fluid Mech.*, 259:333–344, 1994.

[11] M. S. Longuet-Higgins and D. G. Dommermuth. Crest instabilities of gravity waves. Part 2. Nonlinear development and breaking. *J. Fluid Mech.*, 336:33–50, 1997.

[12] P. Wang, Y. Yao, and M. Tulin. An efficient numerical tank for non-linear water waves, based on the multi-subdomain approach with BEM. *International Journal for Numerical Methods in Fluids*, 20:1315–1336, 1995.

[13] L. Jiang, H.-J. Lin, W. W. Schultz, and M. Perlin. Unsteady ripple generation on steep gravity-capillary waves. *J. Fluid Mech.*, 386:281–304, 1999.

[14] H. D. Ceniceros and T. Y. Hou. Dynamic generation of capillary waves. *Phys. Fluids*, 11(5):1042–1050, 1999.

[15] R. C. Y. Mui and D. G. Dommermuth. The vortical structure of parasitic capillary waves. *J. Fluids Eng.*, 117:355–361, 1995.

[16] H. A. Stone and L. G. Leal. The effects of surfactants on drop deformation and breakup. *J. Fluid Mech.*, 220:161–186, 1990.

[17] A. W. Adamson. *Physical Chemistry of Surfaces.* John Wiley & Sons, New York, 1976.

[18] C. Pozrikidis. Numerical studies of cusp formation at fluid interfaces in Stokes flow. *J. Fluid. Mech.*, 357:29–57, 1998.

[19] M. Siegel. Influence of surfactants on rounded and pointed bubbles in two-dimensional Stokes flow. *SIAM J. Appl. Math.*, 59(6):1998–2027, 1999.

[20] H. Wong, D. Rumschtzki, and C. Maldarelli. On the surfactant mass balance at a deforming fluid interface. *Phys. Fluids*, 8(11):3203–3204, 1996.

[21] S. O. Unverdi and G. Tryggvason. A front-tracking method for viscous, incompressible, multifluid flows. *J. Comput. Phys.*, 100:25–37, 1992.

[22] G. Tryggvason, B. Bunner, A. Esmaeeli, D. Juric, N. Al-Rawahi, W. Tauber, J. Han, S. Nas, and Y.-J. Jan. A front-tracking method for computations of multiphase flow. *J. Comput. Phys.*, 169:708–759, 2001.

[23] S. Osher and J. A. Sethian. Fronts propagating with curvature dependent speed: Algorithms based on Hamilton-Jacobi formulations. *J. Phys. Fluids*, 79:12–49, 1988.

[24] M. Sussman, P. Smereka, and S. Osher. A level set approach for computing solutions to imcompressible two-phase flow. *J. Comput. Phys.*, 114:146–159, 1994.

[25] C. S. Peskin. Numerical analysis of blood flow in the heart. *J. Comput. Phys*, 25:220–252, 1977.

[26] G. Baker and A. Nachbin. Stable methods for vortex sheet motion in presence of surface tension. *SIAM J. Sci. Comput.*, 19(5):1737–1766, 1998.

[27] T. Y. Hou, J. S. Lowengrub, and M. J. Shelley. Removing the stiffness from interfacial flows with surface tension. *J. Comput. Phys.*, 114:312–338, 1994.

[28] R. Peyret and T. D. Taylor. *Computational Methods for Fluid Flow.* Springer Verlag, New York, 1983.

[29] P. M. De Zeeuw. Matrix-dependent prolongation and restrictions in a blackbox multigrid solver. *J. Comput. Applied Math.*, 33(1):1–27, 1990.

[30] M. Kang, R. Fedkiw, and X.-D. Liu. A boundary condition capturing method for multiphase

incompressible flow. *J. Sci. Computing*, 15:323–360, 2000.

[31] C. W. Shu and S. Osher. Efficient implementation of essencially non-oscillatory shock capturing schemes. *J. Comput. Phys.*, 77:439–471, 1988.

[32] M. S. Longuet-Higgins and E. D. Cokelet. The deformation of steep surface waves on water I. A numerical method of computation. *Proc. R. Soc. Lond. A.*, 350:1–26, 1976.

[33] K. Okuda. Internal flow structure of short wind waves. Part I. On the internal vorticity structure. *J. Oceanogr. Soc. Jpn.*, 38:28–42, 1982.

[34] M. S. Longuet-Higgins. Capillary rollers and bores. *J. Fluid Mech.*, 240:659–679, 1992.

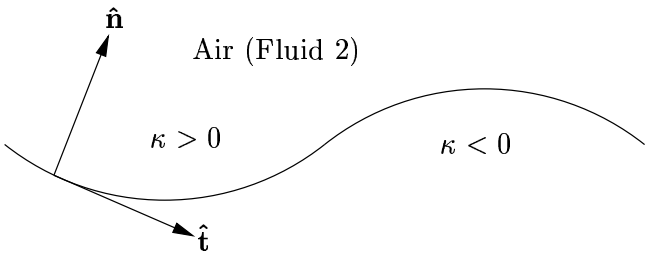

FIG. 1: Schematic of the problem and definition of tangential and normal vectors, and curvature (κ).

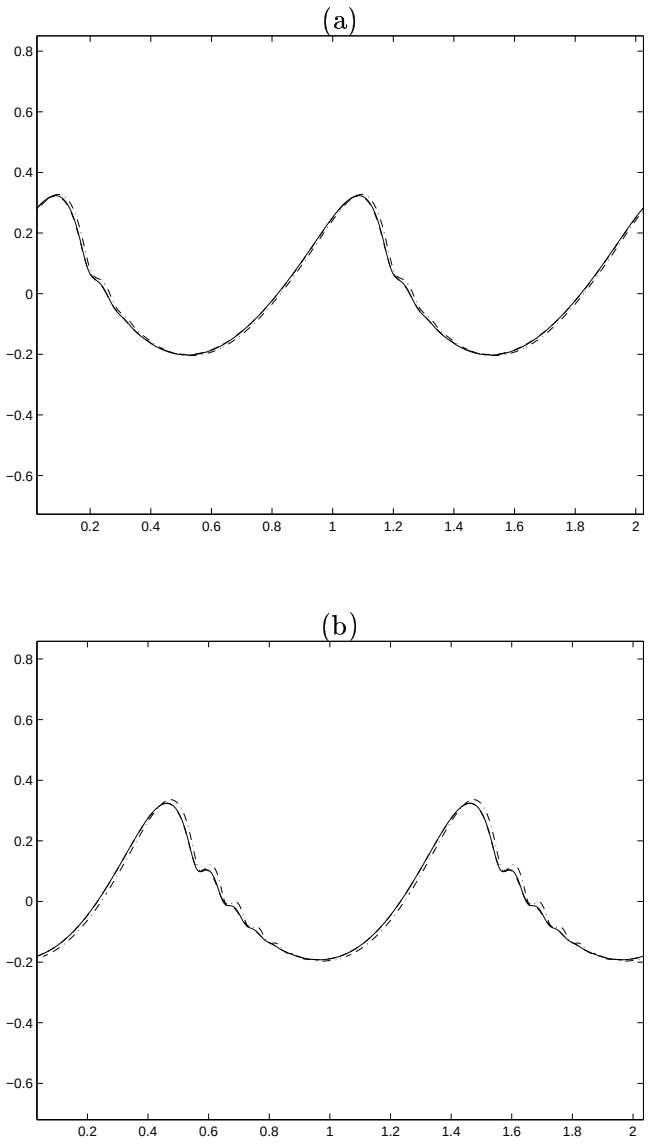

FIG. 2: Profile of a 6.5cm wave with linear wave initial conditions and initial steepness equal to 0.2 at (a) $t = T$ and (b) $t = \frac{11}{8}T$. Shown in solid curve are the two-fluid flow profiles obtained with resolutions 512×512 with 512 interface markers and 1024×1024 with 1024 interface markers. The dashed-dotted profile is the boundary integral simulation of the corresponding potential flow. The vertical scale is eight times the horizontal one.

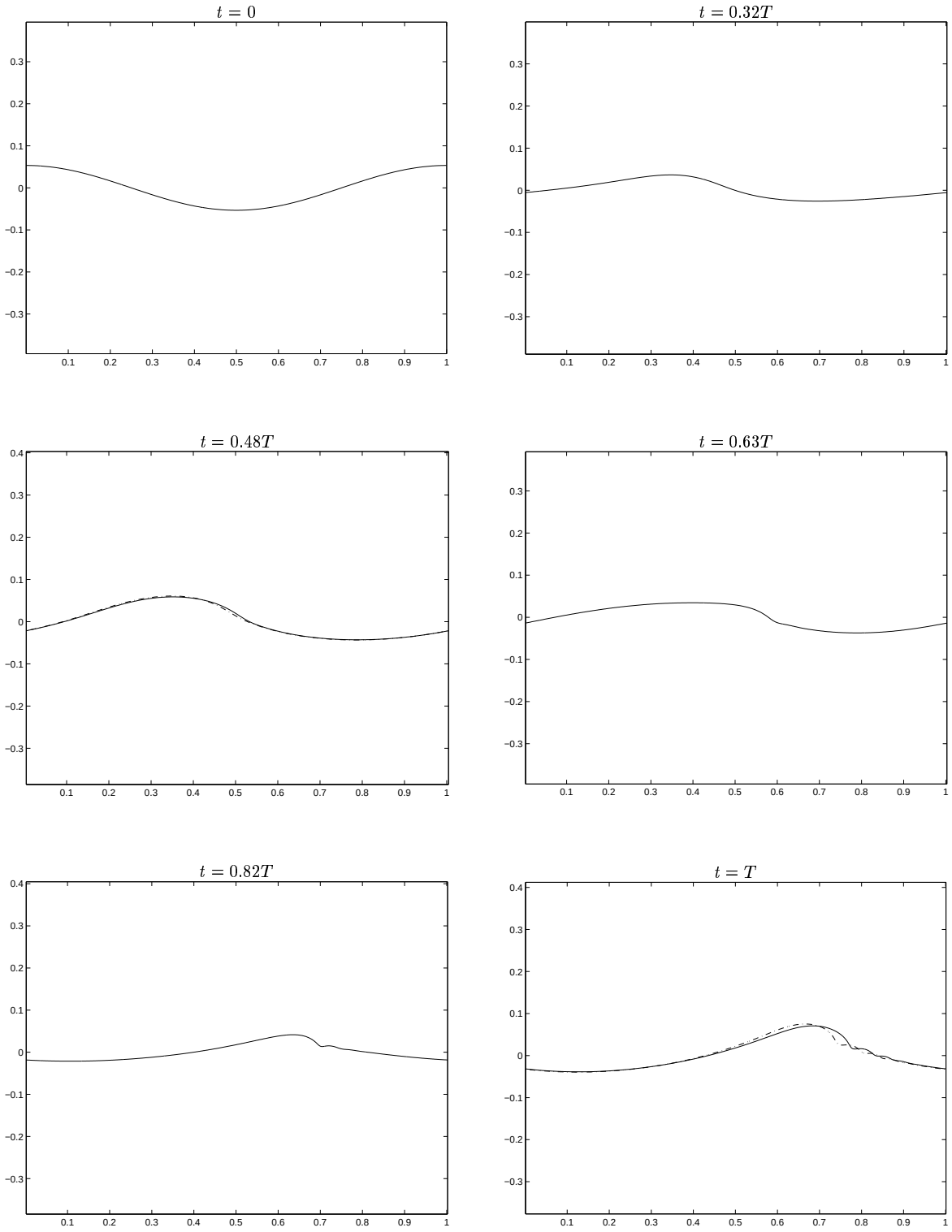

FIG. 3: Wave profile at different times in the absence of surfactants. The potential inviscid flow profile is also shown at $t = 0.48T$ and $t = T$ as a dashed-dotted curve.

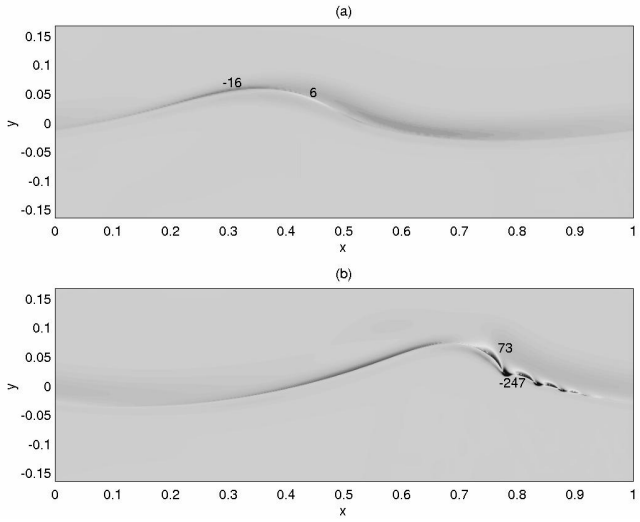

FIG. 4: Vorticity field ω before and after the formation of capillary waves in the absence of surfactants. (a) $t = 0.4T$, $\max\omega = 6$ (crest front), $\min\omega = -16$ (crest back) and (b) $t = T$, $\max\omega = 73$ (at roller), $\min\omega = -247$ (at the toe).

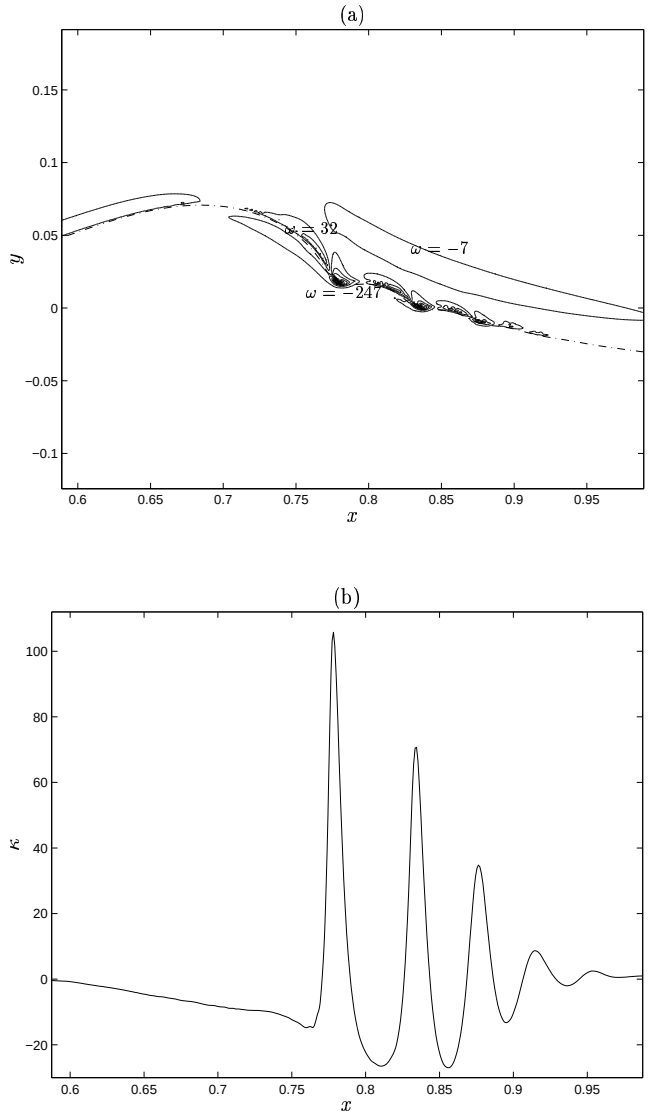

FIG. 5: Close up around the capillary region at $t = T$ of (a) vorticity contours (the position of free surface is shown with a dashed-dotted curve) and (b) the curvature.

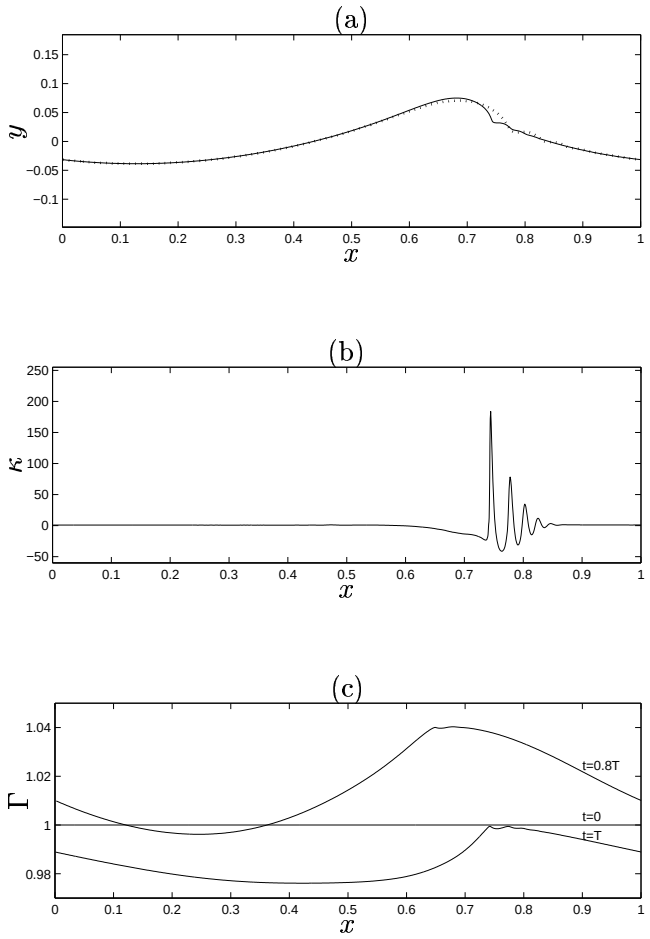

FIG. 6: $\beta = 0.5$ and $Pe = 1$ shown are (a) the wave profile compared with the uniform surface tension (dotted curve) profile at $t = T$, (b) the curvature at $t = T$, and (c) the surfactant concentration at $t = 0$, $t = 0.8T$, and $t = T$.

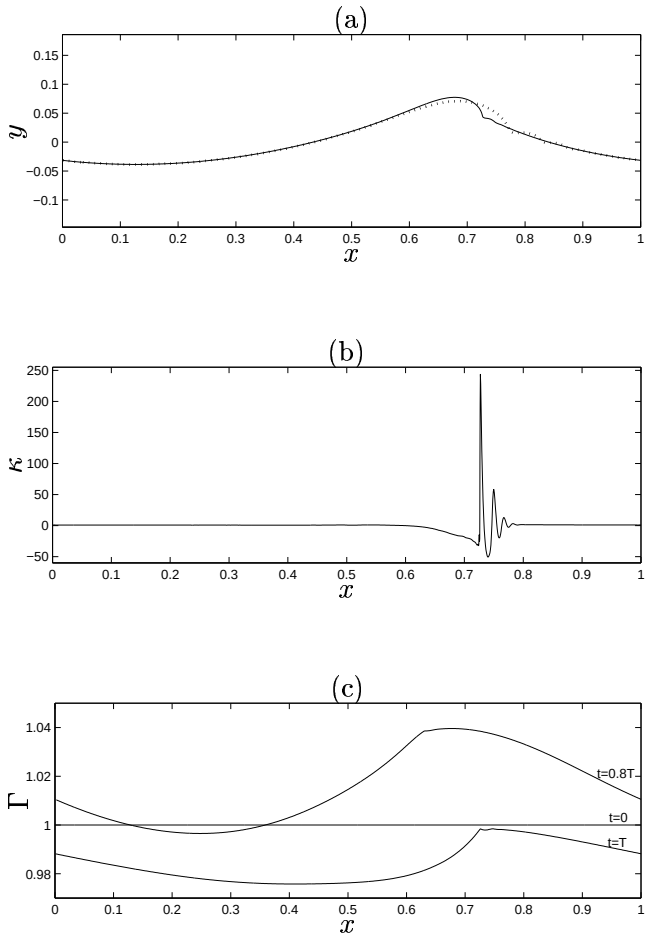

FIG. 7: $\beta = 0.7$ and $Pe = 1$ shown are (a) the wave profile compared with the uniform surface tension (dotted curve) profile at $t = T$, (b) the curvature at $t = T$, and (c) the surfactant concentration at $t = 0$, $t = 0.8T$, and $t = T$.

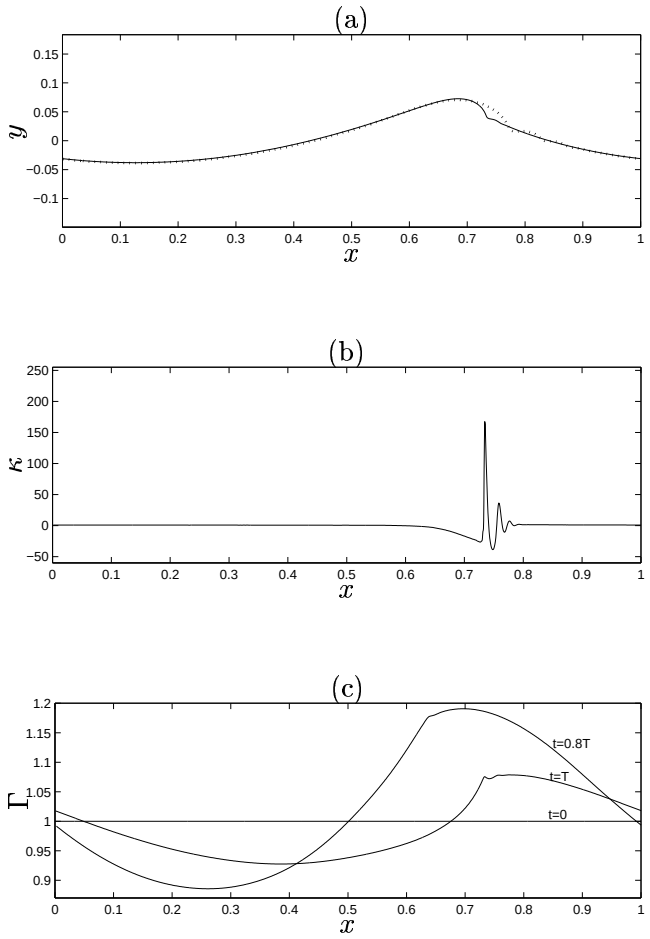

FIG. 8: $\beta = 0.7$ and $Pe = 10$ shown are (a) the wave profile compared with the uniform surface tension (dotted curve) profile at $t = T$, (b) the curvature at $t = T$, and (c) the surfactant concentration at $t = 0$, $t = 0.8T$, and $t = T$.

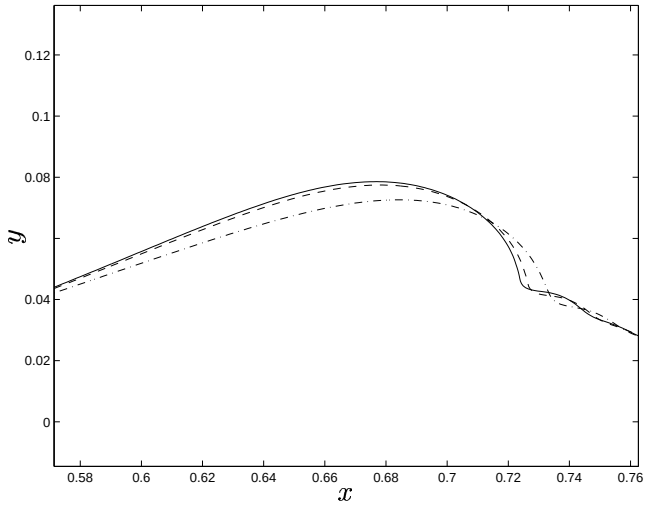

FIG. 9: Comparison of the $\beta = 0.7$ profiles, $Pe = 1$ (dashed curve) and $Pe = 10$ (dashed-dotted curve), with the constant surface tension profile with Weber number $We^* = We/0.3$ (continuous curve).

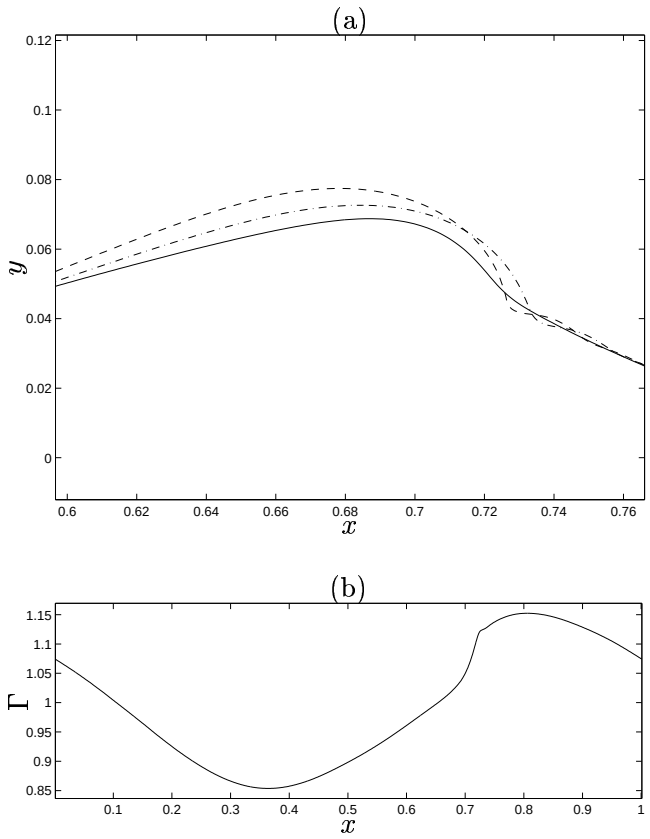

FIG. 10: (a) The $Pe = 100$ profile (continuous curve) compared with the $Pe = 1$ (dashed curve) and $Pe = 10$ (dashed-dotted curve) profiles for fixed $\beta = 0.7$ at $t = T$. and (b) its surfactant concentration also at $t = T$, plotted with equal aspect ratio.

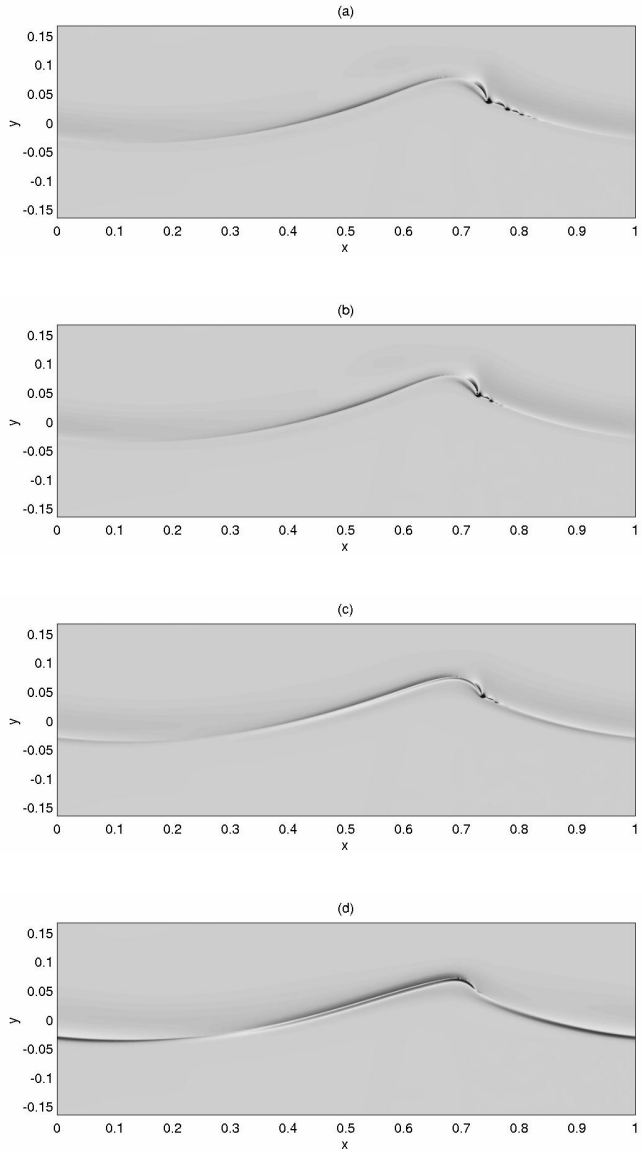

FIG. 11: Vorticity field at $t = T$ for (a) $\beta = 0.5$ and $Pe = 1$, (b) $\beta = 0.7$ and $Pe = 1$, (c) $\beta = 0.7$ and $Pe = 10$, and (d) $\beta = 0.7$ and $Pe = 100$.

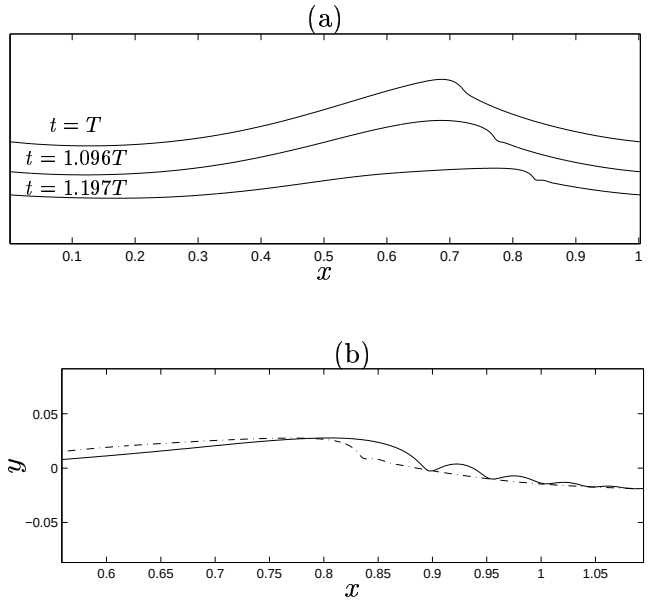

FIG. 12: (a) Wave profile at three different times for $\beta = 0.7$ and $Pe = 100$. (b) Comparison of the $\beta = 0.7$, $Pe = 100$ profile (dashed-dotted curve) with the constant tension We=980 profile (continuous curve).